CrossMark

The Optical Afterglow of GW170817: An Off-axis Structured Jet and Deep Constraints on a Globular Cluster Origin

W. Fong[1], P. K. Blanchard[1,2], K. D. Alexander[1,17], J. Strader[3], R. Margutti[1], A. Hajela[1], V. A. Villar[2], Y. Wu[4], C. S. Ye[1], E. Berger[2], R. Chornock[5], D. Coppejans[1], P. S. Cowperthwaite[6,18], T. Eftekhari[2], D. Giannios[7], C. Guidorzi[8], A. Kathirgamaraju[7,9], T. Laskar[10], A. Macfadyen[4], B. D. Metzger[11], M. Nicholl[12,13], K. Paterson[1], G. Terreran[1], D. J. Sand[14], L. Sironi[11], P. K. G. Williams[2,15], X. Xie[16], and J. Zrake[11]

[1] Center for Interdisciplinary Exploration and Research in Astrophysics and Department of Physics and Astronomy, Northwestern University, 2145 Sheridan Road, Evanston, IL 60208-3112, USA
[2] Center for Astrophysics|Harvard & Smithsonian, 60 Garden Street, Cambridge, MA 02138-1516, USA
[3] Center for Data Intensive and Time Domain Astronomy, Department of Physics and Astronomy, Michigan State University, East Lansing, MI 48824, USA
[4] Center for Cosmology and Particle Physics, New York University, 726 Broadway New York, NY 10003, USA
[5] Astrophysical Institute, Department of Physics and Astronomy, 251B Clippinger Lab, Ohio University, Athens, OH 45701, USA
[6] Observatories of the Carnegie Institute for Science, 813 Santa Barbara Street, Pasadena, CA 91101-1232, USA
[7] Department of Physics and Astronomy, Purdue University, 525 Northwestern Avenue, West Lafayette, IN 47907, USA
[8] Dipartimento di Fisica, Università Ferrara, Via Paradiso 12, I-44100 Ferrara, Italy
[9] Department of Astronomy and Theoretical Astrophysics Center, University of California Berkeley, Berkeley, CA 94720, USA
[10] Department of Physics, University of Bath, Claverton Down, Bath BA2 7AY, UK
[11] Department of Physics and Columbia Astrophysics Laboratory, Columbia University, New York, NY 10027, USA
[12] Institute for Astronomy, University of Edinburgh, Royal Observatory, Blackford Hill EH9 3HJ, UK
[13] Birmingham Institute for Gravitational Wave Astronomy and School of Physics and Astronomy, University of Birmingham, Birmingham B15 2TT, UK
[14] Steward Observatory, University of Arizona, 933 North Cherry Avenue, Tucson, AZ 85721-0065, USA
[15] American Astronomical Society, 1667 K Street NW, Suite 800, Washington, DC 20006-1681, USA
[16] Mathematical Sciences and STAG Research Centre, University of Southampton, Southampton SO17 1BJ, UK

Abstract

We present a revised and complete optical afterglow light curve of the binary neutron star merger GW170817, enabled by deep *Hubble Space Telescope* (*HST*) F606W observations at ≈584 days post-merger, which provide a robust optical template. The light curve spans ≈110–362 days, and is fully consistent with emission from a relativistic structured jet viewed off-axis, as previously indicated by radio and X-ray data. Combined with contemporaneous radio and X-ray observations, we find no spectral evolution, with a weighted average spectral index of $\langle \beta \rangle = -0.583 \pm 0.013$, demonstrating that no synchrotron break frequencies evolve between the radio and X-ray bands over these timescales. We find that an extrapolation of the post-peak temporal slope of GW170817 to the luminosities of cosmological short gamma-ray bursts matches their observed jet break times, suggesting that their explosion properties are similar, and that the primary difference in GW170817 is viewing angle. Additionally, we place a deep limit on the luminosity and mass of an underlying globular cluster (GC) of $L \lesssim 6.7 \times 10^3\, L_\odot$, or $M \lesssim 1.3 \times 10^4\, M_\odot$, at least 4 standard deviations below the peak of the GC mass function of the host galaxy, NGC 4993. This limit provides a direct and strong constraint that GW170817 did not form and merge in a GC. As highlighted here, *HST* (and soon the *James Webb Space Telescope*) enables critical observations of the optical emission from neutron star merger jets and outflows.

Unified Astronomy Thesaurus concepts: Neutron stars (1108); Gravitational waves (678); Gamma-ray bursts (629); Hubble Space Telescope (761)

1. Introduction

The discovery of optical light from the first binary neutron star merger, GW170817 (Abbott et al. 2017a; Arcavi et al. 2017; Coulter et al. 2017; Lipunov et al. 2017; Soares-Santos et al. 2017; Tanvir et al. 2017; Valenti et al. 2017), localized the event to a projected distance of ≈2 kpc from its host galaxy NGC 4993 (Blanchard et al. 2017; Lyman et al. 2017), and provided a precise position for follow-up observations across the electromagnetic spectrum (e.g., Abbott et al. 2017b). Energy released from the radioactive decay of heavy elements synthesized in the merger ejecta (resulting in a "kilonova"; Metzger et al. 2010) dominated the optical emission at early times, and its characterization was primarily led by ground-based observations (Andreoni et al. 2017; Arcavi et al. 2017;

Chornock et al. 2017; Cowperthwaite et al. 2017; Coulter et al. 2017; Díaz et al. 2017; Drout et al. 2017; Kasliwal et al. 2017; Lipunov et al. 2017; Nicholl et al. 2017; Pian et al. 2017; Pozanenko et al. 2017; Smartt et al. 2017; Tanvir et al. 2017; Troja et al. 2017; Utsumi et al. 2017; Valenti et al. 2017; Villar et al. 2017). At a few weeks post-merger, the field became inaccessible to optical facilities. When GW170817 emerged from solar conjunction at ≈100 days, the nonthermal afterglow emission, which results from relativistic material interacting with the surrounding medium, outshined the kilonova. The study of this second phase in the optical band was enabled by the *Hubble Space Telescope* (*HST*; Alexander et al. 2018; Lyman et al. 2018; Margutti et al. 2018; Lamb et al. 2019a; Piro et al. 2019), which was the only facility with the sensitivity to securely detect the source at these epochs, due to a combination of intrinsic faintness of the afterglow and contaminating light from NGC 4993.

Table 1
HST/F606W Afterglow Photometry of GW170817

Mid-time (UT)	δt (days)	Instrument	Exp. Time (s)	AB Mag	F_ν (μJy)	Program ID
2017 Dec 6.022	110.49	WFC3/UVIS2	2264	26.31 ± 0.19	0.110 ± 0.019	14270
2018 Jan 1.573	137.04	ACS/WFC	2120	26.59 ± 0.23	0.084 ± 0.018	15329
2018 Jan 29.721	165.19	WFC3/UVIS	2372	26.50 ± 0.19	0.091 ± 0.016	14607
2018 Feb 5.740	172.21	WFC3/UVIS2	2400	26.58 ± 0.22	0.085 ± 0.017	14771
2018 Mar 14.626	209.10	WFC3/UVIS	2432	26.61 ± 0.26	0.082 ± 0.020	14607
2018 Mar 23.895	218.37	ACS/WFC	2120	26.90 ± 0.31	0.063 ± 0.018	15329
2018 Jun 10.327	296.80	WFC3/UVIS2	5220	27.29 ± 0.35	0.044 ± 0.014	14771
2018 Jul 11.752[a]	328.22	WFC3/UVIS2	14,070	27.58 ± 0.35	0.034 ± 0.011	15482
2018 Jul 20.357	336.83	ACS/WFC	2120	$\gtrsim 27.2$	$\lesssim 0.048$	15329
2018 Aug 14.852[b]	362.32	WFC3/UVIS2	14,070	27.83 ± 0.29	0.027 ± 0.0072	15482
2019 Mar 24.659[c]	584.13	ACS/WFC	26,912	$\gtrsim 28.2$	$\lesssim 0.019$	15606

Notes. Times are quoted in the observer frame. All observations are taken with the F606W filter. Limits correspond to 3σ confidence, and uncertainties correspond to 1σ. Magnitudes are corrected for Galactic extinction (Schlafly & Finkbeiner 2011).
[a] Two separate visits on 2018 July 10 and 13 UT.
[b] Two separate visits on 2018 August 14 and 15 UT.
[c] Two separate visits on 2019 March 21 and 27 UT.

In conjunction with ongoing radio and X-ray campaigns, the optical afterglow probes the relativistic outflow from the merger. Several studies based primarily on the radio and X-ray observations of GW170817 have converged on a structured jet model, in which the bulk of the energy is carried by a relativistic jet, surrounded by less-collimated, slower material (Alexander et al. 2018; Lazzati et al. 2018; Margutti et al. 2018; Mooley et al. 2018a, 2018b; Troja et al. 2018a; Wu & MacFadyen 2018). These studies have also shown that at $\gtrsim 100$ days post-merger, the broadband spectral energy distribution (SED) follows a single power law characterized by $F_\nu \propto \nu^{-0.6}$. Notably, the optical band provides an important anchor between the nine orders of magnitude in frequency from the radio to the X-ray bands.

Thus far, extracting the flux from the optical counterpart of GW170817 has relied upon modeling the surface brightness profile of NGC 4993 and subtracting its contribution. However, the morphology of NGC 4993 is complex and characterized by dust lanes and concentric shells (Blanchard et al. 2017; Levan et al. 2017; Palmese et al. 2017), making accurate and uniform photometry extremely challenging. Thus, previous studies that utilized optical data suffer from a combination of imperfect galaxy subtraction and nonuniform photometric methods (Alexander et al. 2018; Lyman et al. 2018; Margutti et al. 2018; Lamb et al. 2019a; Piro et al. 2019).

Here, we present a deep *HST*/F606W observation of GW170817 at ≈ 584 days, which serves as the first robust optical template for the late-stage afterglow emission, against which we can subtract earlier epochs. This enables reliable and uniform photometry of the optical afterglow for the first time. We use the observation to produce a complete and revised light curve of the optical afterglow in the F606W filter, as well as a direct and strong limit on an underlying globular cluster (GC) to constrain the formation of its progenitor. In the following sections, we present the new and archival observations used in this study (Section 2), the details of the image subtraction and broadband spectral fitting (Section 3), a discussion of the afterglow properties in the context of short gamma-ray bursts (GRBs) and the limit with respect to the GC mass function of NGC 4993 (Section 4), and concluding remarks (Section 5).

All magnitudes in this Letter are in the AB system and corrected for a Galactic extinction of $(E(B - V) = 0.109;$ Schlafly & Finkbeiner 2011). Reported uncertainties correspond to 68% confidence. We employ a standard ΛCDM cosmology with $\Omega_M = 0.286$, $\Omega_\Lambda = 0.714$, and $H_0 = 69.6 \, \text{km s}^{-1} \, \text{Mpc}^{-1}$ (Bennett et al. 2014). We adopt a distance to both NGC 4993 and the afterglow of $D_L = 40.7 \, \text{Mpc}$ (Cantiello et al. 2018).

2. Observations

2.1. A Deep F606W Observation

We obtained *HST* observations of GW170817 with the Advanced Camera for Surveys (ACS) under Program 15606 (PIs: Fong, Margutti). The observations were performed in the F606W filter over two visits on 2019 March 21 UT and 2019 March 27 UT for a total on-source time of 26,912 s (six orbits).

We retrieve calibrated FLC images from the Mikulski Archive for Space Telescopes (MAST) archive,[19] precorrected for charge transfer efficiency. We used tasks as part of the Drizzlepac software package (Gonzaga 2012) and IRAF (Tody 1986, 1993) to process the data. We used the astrodrizzle task to create a combined drizzled image for each visit, using final_scale=0″.05 pixel^{-1} and final_pixfrac = 0.8, and then aligned the images to a common early epoch using the tweakreg task (described in Section 3.1) with relative astrometric uncertainties of ≈ 6.5–8.0 mas (≈ 0.1–0.2 *HST* pixels). We used IRAF/imcombine to combine the images from both visits. The mid-time of the final combined image corresponds to $\delta t \approx 584.1$ days, where δt is the time since the gravitational-wave trigger (2017 August 17 at 12:41:04 UT; Abbott et al. 2017a).

2.2. Archival Observations

Since our study concentrates on the optical afterglow emission of GW170817, we retrieve images from MAST taken with ACS and the Wide Field Camera 3 (WFC3) in the F606W
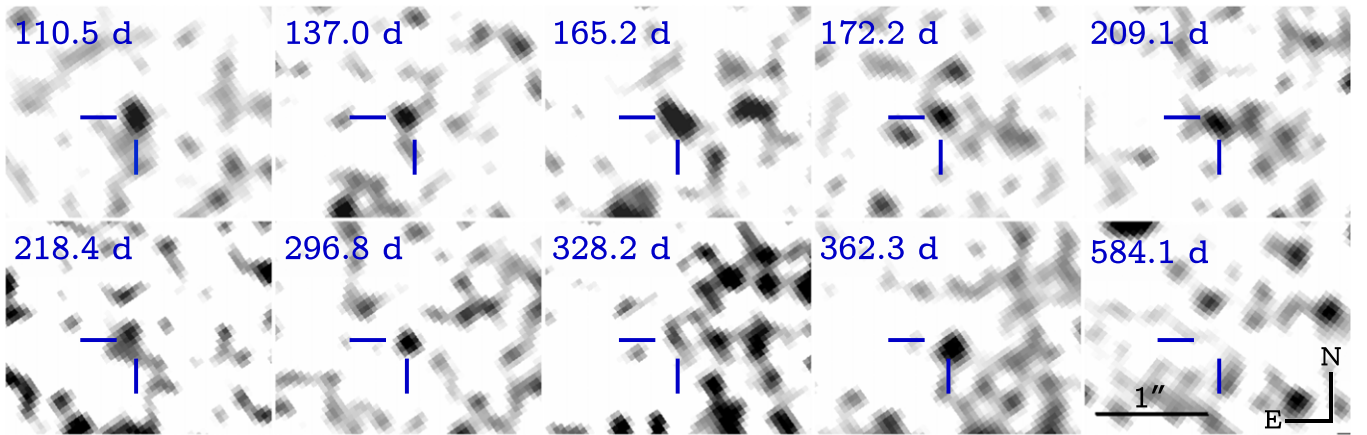
Figure 1. `HOTPANTS` residual images from image subtraction between nine epochs of *HST*/ACS F606W imaging and the template observation obtained on 2019 March 21–27 UT (Program 15606). The last panel at $\delta t = 584.1$ days is the median-subtracted template. The position of the afterglow at $\delta t = 110.5$ days is denoted by the blue crosshairs in all panels. The afterglow is detected at the $\gtrsim 3\sigma$ level in all residual images pictured here, while the template exhibits no source at the afterglow position to $m_{\rm F606W} \gtrsim 28.2$ mag. The scale and orientation of all images are denoted in the last panel, and all images have been smoothed with a 3 pixel Gaussian kernel.

filter at $\gtrsim 100$ days. The observations comprise 10 epochs spanning 2017 December 6 to 2018 August 14 UT, corresponding to $\delta t \approx 110.5$–362.3 days. The details of all of the *HST*/F606W observations are displayed in Table 1. Results from these observations were previously reported in Alexander et al. (2018), Margutti et al. (2018), Lyman et al. (2018), Troja et al. (2019b), Lamb et al. (2019a), and Piro et al. (2019).

We processed all images in the same manner as described in Section 2.1. For observations taken within a few days of each other with the same instrument, we combine the visits to increase the signal-to-noise ratio and report them as a single epoch. In addition to our 2019 March observations, this also applies to observations over 2018 July 10–13 UT and 2018 August 14–15 UT.

3. Analysis and Results

3.1. Astrometry

We performed absolute astrometry of the first epoch in our sequence, 2017 December 6 UT, to the Pan-STARRS 1 catalog (Chambers et al. 2016) using 33 point sources in common with IRAF/`ccmap` and `ccsetwcs`. The resulting absolute astrometric tie uncertainty is $0\overset{''}{.}039$ (1σ). We align all subsequent images to this epoch using the `tweakreg` task as part of the Drizzlepac package, which uses common sources to align the images in WCS to subpixel precision. For each image, `tweakreg` uses 83–147 sources, with a relative astrometric tie error range of 4.8–11.0 mas. Using Source Extractor (Bertin & Arnouts 1996), we derive an afterglow position based on the 2017 December 6 epoch of $\alpha = 13^{\rm h}09^{\rm m}48\overset{\rm s}{.}07$ and $\delta = -23°22'53\overset{''}{.}37$ (J2000) with an uncertainty of $0\overset{''}{.}040$ (including a positional uncertainty for the afterglow centroid of 8.7 mas). This position is consistent with that of the kilonova (e.g., Soares-Santos et al. 2017), and we use it for our subsequent photometric analysis.

3.2. A New Template

To measure the upper limit on the afterglow at the position of GW170817 in the 2019 March observation, we first subtract off the smooth galaxy background that we model with a Sérsic surface brightness profile using the `GALFIT` software package

(Peng et al. 2010). In `GALFIT` we employ a point-spread function (PSF) empirically determined from stars in the image using IRAF/`daophot`. We use IRAF/`addstar` to inject artificial point sources at the position of GW170817 in the `GALFIT` residual image, with the PSF determined above. We then perform photometry on each injected source using a $0\overset{''}{.}2$ aperture and apply the appropriate aperture correction to correct to infinity (Sirianni et al. 2005). We repeat the experiment with sources of varying brightness to determine the flux level that would be recovered at the 3σ level, resulting in a 3σ upper limit of $m_{\rm F606W} \gtrsim 27.6$ at the position of GW170817.

As previously discussed in Blanchard et al. (2017), a Sérsic galaxy model provides an inadequate description of the galaxy light, which exhibits large-scale shell structure and dust lanes, apparent in the residuals and in the resulting goodness-of-fit value ($\chi_\nu^2 = 332$ for 4,374,194 d.o.f.). This structure, along with the small-scale brightness fluctuations, are known limitations for deriving a limit with the galaxy subtraction method.

Given the limitations of the simple analytic model of the galaxy light, we explore an alternative method to subtract the background to improve our limit. We apply a median filter to the original image using a 30×30 pixel box (corresponding to $1\overset{''}{.}5$ or ≈ 0.29 kpc on a side) using IRAF/`median`, where the box size is chosen so that no evidence of structure on the scale of the PSF is detectable in the median-filtered image. We then subtract the median-filtered image from the original image to produce a median-subtracted image suitable for photometry (Figure 1).

We perform photometry of faint sources in the median-subtracted images using IRAF/`phot`, finding a 3σ limit of $m_{\rm F606W} \gtrsim 28.2$ mag. We also inject fake point sources at the position of GW170817 using the empirically derived PSF from the full image and recover a similar limit. To check the sensitivity of the result to the details of the filter, we also produce similar median-subtracted images made with 40 and 50 pixel filters. The final limit is not sensitive to these details, demonstrating that this method is robust. We use this limit for the remainder of our analysis, since the nondetection of any source to this limit makes this image suitable as a template.
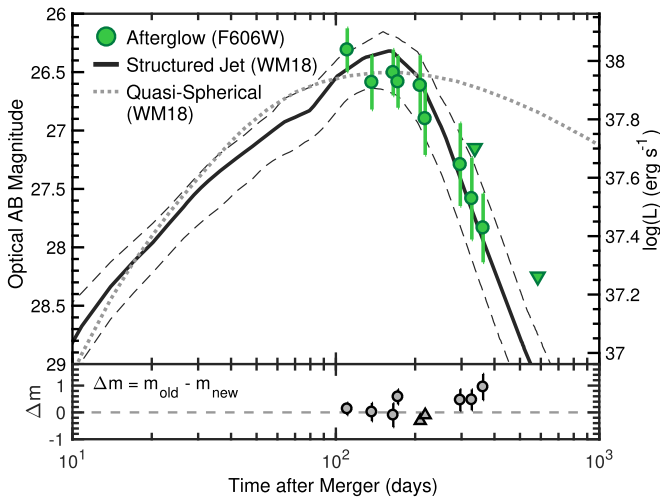
Figure 2. Top: *HST*/F606W light curve of the afterglow of GW170817 spanning ≈110.5–584.1 days (green points; observer frame); downward triangles denote 3σ upper limits. The upper limit at ≈584.1 days is measured from the median-subtracted image, while all other data points are measured from HOTPANTS residual images. Also shown are a structured jet model and the range of light curves describing the top 5% of models (black solid and dotted–dashed lines), and a quasi-spherical outflow model (dotted line; Wu & MacFadyen 2018). Bottom: magnitude difference, Δ*m*, between published values in previous works (Alexander et al. 2018; Lyman et al. 2018; Margutti et al. 2018; Lamb et al. 2019a; Piro et al. 2019) and the new values measured in this work. Upward triangles denote epochs that were previously reported as upper limits, and are now detected in this work.

Figure 3. Broadband SED of the afterglow of GW170817 at nine epochs of our *HST* observations, spanning ≈110–584 days; fluxes are scaled for clarity. The *HST* photometry in this paper (green circles), radio afterglow (red squares; Margutti et al. 2018; Mooley et al. 2018c; Dobie et al. 2018; Mooley et al. 2018b; Alexander et al. 2018; Troja et al. 2019b; A. Hajela et al. 2019, in preparation), and X-ray afterglow (blue diamonds; A. Hajela et al. 2019, in preparation) are shown. The gray lines are best-fit power laws to the data at each epoch. 1σ uncertainties are plotted, but the large majority are smaller than the size of the symbols.

3.3. Image Subtraction and Afterglow Photometry

We use the HOTPANTS software package (Becker 2015) to subtract the 2019 March original image from each of the earlier epochs, and convolve each residual image to the pixel scale of the template (0.″05 pixel^{-1}). The residual images are shown in Figure 1. Although the majority of imaging was performed with the UVIS detector, and the template is taken with ACS, the difference in photometric calibration between ACS and UVIS is negligible in the F606W filter compared to the measured uncertainties in afterglow photometry (see below), with typical differences of ≲0.04 mag (Deustua & Mack 2017). Thus, we can reliably perform aperture photometry directly on the residual images.

Using the IRAF/phot package, we perform aperture photometry of the afterglow. We use a 0.″3 aperture corresponding to 2.5 × FWHM, fixed at the position of the afterglow in all epochs. For each of the ACS epochs, we calculate aperture corrections by performing photometry in 0.″3 and 0.″5 radius apertures for 10–12 bright, unsaturated stars in each of the original fields, resulting in initial corrections of ≈0.01–0.03 mag. We then apply tabulated encircled energy corrections to correct the 0.″5 apertures to infinity (Bohlin 2016). For UVIS, we use the tabulated corrections[20] to correct the 0.″3 radius apertures to infinity, typically ≈0.11–0.13 mag.

In all except the epoch at ≈336.8 days (2018 July 20), a source at the afterglow position is detected at the ≳3σ level. The nondetection in that single epoch is unsurprising given the relatively shallow depth of the image (Table 1). To derive the upper limit for this epoch, we perform aperture photometry of faint sources near the position of the afterglow. The resulting photometry is listed in Table 1 and is displayed in Figure 2. For
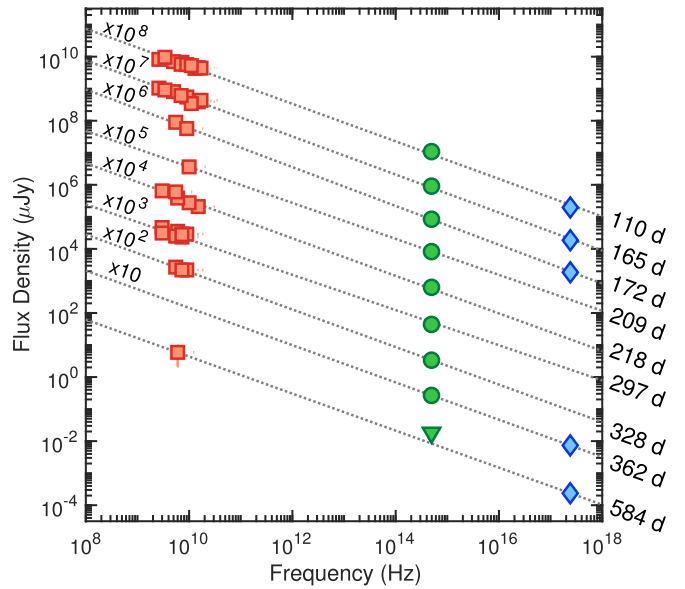
comparison, we also show the structured jet and quasi-spherical models that best fit the radio through X-ray evolution to ≈260 days (Wu & MacFadyen 2018).

3.4. Broadband Afterglow Fitting

To place the *HST* photometry in the context of the broadband afterglow and quantify the broadband spectral evolution at δ*t* ≳ 100 days, we collect fluxes from the literature in the radio and X-ray bands at contemporaneous epochs, defined here to be within ±10 days of *HST* observations. In the radio band, there are available data for all epochs except at δ*t* ≈ 137, 337, and 362 days. The data are taken with the Karl G. Jansky Very Large Array (VLA) and the Australia Telescope Compact Array (ATCA), spanning 2.5–17 GHz (Alexander et al. 2018; Dobie et al. 2018; Margutti et al. 2018; Mooley et al. 2018a, 2018b, 2018c; Troja et al. 2019b). We also use a 6 GHz VLA observation at δ*t* ≈ 585 days, presented in A. Hajela et al. (2019, in preparation).

In the X-ray band, we find relevant comparison *Chandra X-ray Observatory* observations at five epochs. Previous analyses of these observations have appeared in Nynka et al. (2018), Margutti et al. (2018), Troja et al. (2018a, 2019b), Pooley et al. (2018), Ruan et al. (2018), and Lin et al. (2019). Here, we use the fluxes and spectral parameters calculated in A. Hajela et al. (2019, in preparation), which serve as a uniform analysis of all available *Chandra* data of the X-ray afterglow of GW170817 to ≈583.1 days. To enable comparison of the X-ray observations to the optical and radio data, we convert the 0.3–10 keV X-ray fluxes to flux densities, $F_{\nu,\,X}$, at a fiducial energy of 1 keV, using the derived photon index, Γ, at each epoch, where $F_{\nu,X} \propto \nu^{\beta_X}$ and $\beta_X \equiv 1 - \Gamma$. The radio and X-ray data, along with our *HST* photometry, are displayed in Figure 3.

Table 2
Broadband Spectral Index β

δt[a] (d)	β	Data Reference[b]
110.49	$-0.586^{+0.024}_{-0.044}$	1–3
165.19	$-0.594^{+0.032}_{-0.053}$	1, 3
172.21	$-0.606^{+0.020}_{-0.032}$	3, 4
209.10	$-0.562^{+0.020}_{-0.028}$	5
218.37	$-0.586^{+0.053}_{-0.12}$	5–7
296.80	$-0.549^{+0.057}_{-0.13}$	5–6, 8
328.22	$-0.586^{+0.053}_{-0.097}$	8
362.32	$-0.582^{+0.067}_{-0.057}$	3
584.13	$-0.578^{+0.061}_{-0.040}$	3
All, weighted avg.	-0.583 ± 0.013	

Notes.
[a] This is the epoch of the *HST* observation. Radio and X-ray observations with $\delta t \pm 10$ days were considered contemporaneous and were included in the power-law fits.
[b] Literature references for the plotted radio and X-ray data. All *HST* data points are from this work.
References. (1) Margutti et al. (2018); (2) Mooley et al. (2018c); (3) A. Hajela et al. (2019, in preparation); (4) Dobie et al. (2018); (5) Mooley et al. (2018b); (6) Alexander et al. (2018); (7) Piro et al. (2019); (8) Troja et al. (2019b).

We use χ^2-minimization to fit the broadband spectrum at each epoch to a single power-law model in the form $F_\nu \propto \nu^\beta$, characterized by spectral index β and a flux normalization parameter. We fit all of the available data at each epoch separately. The resulting fits have $\chi^2_\nu \approx 0.6 - 1.3$, demonstrating that the single power-law model is adequate to fit the data over all epochs (Figure 3). The values for β and 1σ uncertainties are given in Table 2, and the temporal evolution is displayed in Figure 4. We calculate a weighted average of the spectral index across all epochs considered here of $\langle\beta\rangle = -0.583 \pm 0.013$.

4. Discussion

4.1. Off-axis Afterglow Properties

We present a revised light curve of the optical afterglow of GW170817, relative to previous studies that have used subsets of *HST* observations to derive measurements and upper limits of the afterglow in the F606W filter (Alexander et al. 2018; Lyman et al. 2018; Margutti et al. 2018; Lamb et al. 2019a; Piro et al. 2019). We calculate the difference Δm between the published values and the values presented in this work (Figure 2). Overall, we find that the afterglow in most epochs is systematically brighter than previously reported, with differences of $\Delta m \approx -0.1$–1 mag between published values and the values presented in this work (Figure 2), and an increase in Δm as the afterglow becomes fainter. Our analysis also recovers a $\gtrsim 3\sigma$ source in two observations that were previously reported as upper limits (Alexander et al. 2018; Piro et al. 2019). The differences with respect to published values are not surprising given the nonuniformity of methods used for both galaxy subtraction and photometry, and the complicated structure of NGC 4993, which makes accurate galaxy subtraction, and thus background estimation, challenging without a proper template.
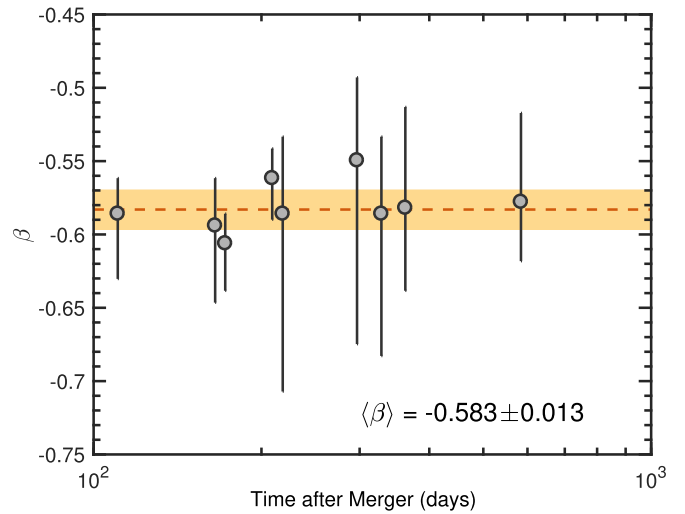
Figure 4. Temporal evolution of the spectral index, β, from fitting the radio, *HST*, and *Chandra* X-ray data. Uncertainties correspond to 1σ, and are produced from the χ^2 fitting procedure. The red dashed line and orange band denote the weighted average and uncertainty across the ≈ 110–584 day interval.

The temporal evolution of the optical afterglow exhibits a flattening at ≈ 110–172 days, followed by a steep decline at $\gtrsim 200$ days (Figure 2). The entire data set can be fit with a broken power law with $\alpha_1 = -0.4 \pm 0.2$ and $\alpha_2 = -2.20 \pm 0.25$ (where $F_\nu \propto t^\alpha$), with a break time of ≈ 200–240 days depending on the smoothness of the break. The large change in slope signifies that we are witnessing the peak, followed by a rapid decline after the jet break (Rhoads 1999). For synchrotron emission, the post-jet-break decline is expected to evolve as $F_\nu \propto t^{-p}$, where p is the electron power-law index describing the input energy distribution of electrons (Sari et al. 1999), and thus we can infer a value of $p = 2.20 \pm 0.25$ from the optical light curve.

We can obtain an independent constraint on p from the spectral behavior of the source. Combined with the radio and X-ray evolution, the afterglow of GW170817 maintains the same spectral index within 1σ uncertainties for the duration of the *HST* observations (Figures 3–4). This demonstrates that the radio, optical, and X-ray bands all lie on the same spectral slope between $\nu_m \lesssim \nu \lesssim \nu_c$ (where ν_m is the peak frequency and ν_c is the cooling frequency of the synchrotron spectrum; e.g., Sari et al. 1998; Granot & Sari 2002) out to ≈ 584 days, and that no break frequencies evolve between the radio and X-ray bands on these timescales. The inferred value of $p = 1 - 2\beta = 2.166 \pm 0.026$ is fully consistent with the value derived from the light curve, as well as with previous works based on broadband data out to ≈ 260 days (Alexander et al. 2018; Margutti et al. 2018; Wu & MacFadyen 2018; Lamb et al. 2019a).

A comparison of the *HST* light curve to models that best fit the radio and X-ray light curves to ≈ 260 days (Alexander et al. 2018; Margutti et al. 2018; Wu & MacFadyen 2018; Kathirgamaraju et al. 2019) demonstrates that the optical emission at $\gtrsim 100$ days is emanating from a relativistic structured jet viewed off-axis (Figure 2). Moreover, models of mildly relativistic quasi-spherical outflows, in which the jet (if produced at all) fails to break out of the ejecta, overpredict the observed optical flux by $\gtrsim 1.5$–4 times at $\gtrsim 200$ days. This provides clear confirmation from the optical emission that we

are viewing an off-axis jet as opposed to a quasi-spherical outflow. This supports previous studies that reached a similar conclusion based primarily on temporal and spectral behavior within a single band (D'Avanzo et al. 2018; Lyman et al. 2018; Mooley et al. 2018b; Nynka et al. 2018; Lamb et al. 2019a) and broadband data (Alexander et al. 2018; Lazzati et al. 2018; Margutti et al. 2018; Troja et al. 2019b; Wu & MacFadyen 2018). This is also corroborated by the detection of super-luminal motion and constraints on the jet size from very long baseline interferometric observations (Mooley et al. 2018a; Ghirlanda et al. 2019), although it has also been shown that the source motion is expected to be indistinguishable between jetted and quasi-spherical models for $\lesssim 300$ days (Zrake et al. 2018).

4.2. Comparison to Short GRB Afterglows

GW170817 represents the first detection of an off-axis optical afterglow, while cosmological short GRBs represent those events seen close to or on-axis. The presence of relativistic jets in both types of events is one of several characteristics that signify a common origin. The similarity in their inferred explosion properties also suggest that the primary difference in behavior between short GRB jets and that of GW170817 is the viewing angle (Fong et al. 2017; Kathirgamaraju et al. 2018; Lazzati et al. 2018; Salafia et al. 2019; Wu & MacFadyen 2019).

Here, we explore this in another way by connecting the optical properties of GW170817 with short GRBs. If GW170817 and cosmological short GRBs share the same values for their explosion properties, in particular a combination of the jet opening angle, kinetic energy, and circumburst density, then regardless of observer angle, the post-jet-break behavior of their afterglows should asymptote to the same declining light curve at late times (van Eerten & MacFadyen 2012). In this case, an extrapolation of the post-peak decline of GW170817 should intersect with the short GRB population at their expected jet break times in luminosity space.

We collect data of all short GRBs with multiple optical afterglow detections, comprising 25 events (updated from Fong et al. 2015, and including the afterglow and kilonova of the short GRB 160821B; Lamb et al. 2019b; Troja et al. 2019a). We use the burst redshifts to obtain the afterglow luminosities as a function of rest-frame time, assuming $z = 0.5$ (the median value of the population; Berger 2014; Fong et al. 2017) for bursts without determined redshifts. The short GRB light curves are shown in Figure 5, highlighting the single source with a jet break measured in the optical band (GRB 130603B; Fong et al. 2014). The extrapolation of the post-peak slope of $\alpha \approx -p \approx -2.17$ from GW170817 intersects short GRBs at ≈ 0.7–4 days (rest-frame). Indeed, the short GRBs with measured jet breaks have a range of jet break times that are similar, ≈ 0.4–3.5 days (Figure 5; Burrows et al. 2006; Soderberg et al. 2006; Fong et al. 2012, 2014; Troja et al. 2016). This simple exercise is consistent with the notion that the combination of jet opening angle, kinetic energy, and circumburst density of GW170817 are similar to the population of short GRBs. As learned from short GRBs, we expect there to be inherent diversity in these properties that will manifest itself as a spread in behavior (Fong et al. 2015).

A further comparison of optical emission from short GRBs to the kilonova of GW170817 (compiled in Villar et al. 2017) clearly demonstrates that for on-axis events, short GRB
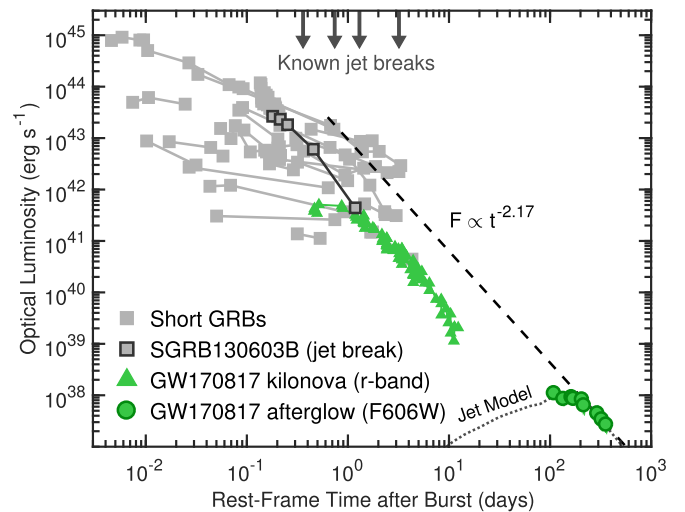
Figure 5. Afterglow (this work) and *r*-band kilonova (compiled in Villar et al. 2017, see references in text) of GW170817 along with the structured jet model (dotted line; Wu & MacFadyen 2018). Also shown are 25 short GRBs with optical afterglow light curves; GRB 130603B is the single known jet break in the optical band and is highlighted. Arrows from the top denote the rest-frame jet break times of four short GRBs. The extrapolation of the post-peak slope of GW170817 ($\alpha = -2.17$) back to the luminosities of short GRBs intersects the population at ≈ 0.7–4 days.

afterglows are likely to outshine their optical kilonovae at all epochs if the luminosity and evolution of GW170817 are representative of the population. However, the overlap between the kilonova of GW170817 and the low-luminosity end of the short GRB distribution, including the claimed kilonovae in the short GRBs 150101B and 160821B (Troja et al. 2018b; Lamb et al. 2019b; Troja et al. 2019a) leaves open the possibility that a small subset of short GRBs are discovered slightly off-axis, and the optical emission is in fact dominated by the kilonova in these cases. Finally, Figure 5 shows that if GW170817 had not been in solar conjunction at ≈ 15–100 days, we would have been able to witness the rise of the optical afterglow starting at ≈ 20 days and potentially the intersection with the kilonova emission.

4.3. Constraints on a Globular Cluster Origin

We now explore GW170817 in the context of its progenitor formation. Previous studies have used the stellar mass, stellar population age, star formation history of NGC 4993, and the location of GW170817 with respect to the host galaxy center, to infer properties of the progenitor system, including the kick velocity, helium-star mass, and initial separation (Abbott et al. 2017c; Blanchard et al. 2017). Overall, these studies found consistency between the progenitor properties and the distributions of Galactic binary neutron stars that formed via isolated binary evolution (e.g., Wong et al. 2010). On the other hand, early simulations of interactions in GCs have suggested that their dense stellar environments can also provide a significant channel of neutron star mergers and short GRBs, through dynamical encounters, tidal capture, or in-cluster primordial evolution (e.g., Grindlay et al. 2006; Ivanova et al. 2008; Lee et al. 2010). Moreover, the observed double neutron star system B2127+11C in the GC M15 is expected to merge within a Hubble time (Anderson et al. 1990; Tauris et al. 2017), motivating a search for a GC at or near the position of GW170817.
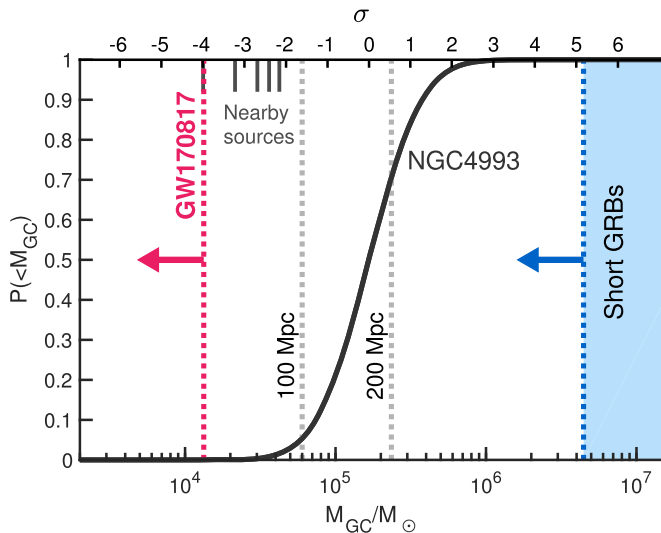
Figure 6. GCMF of the host galaxy NGC 4993 (black line), derived from the GCLF (Lee et al. 2018), compared to various limits: the limit at the position of GW170817 on a star cluster of $\lesssim 1.3 \times 10^4\, M_\odot$ (red dotted line), upper limits from $z \lesssim 0.3$ SGRBs (blue region), and the limits on GCs for similarly deep *HST* observations for events at 100 and 200 Mpc (dotted gray lines). Also shown are the corresponding masses of nearby objects (if they are GCs) at the distance of GW170817 (gray lines from top). The top axis denotes the σ from the mean of the NGC 4993 GCMF for a Gaussian distribution. Compared to the GCMF, the observations rule out a cluster at the position of GW170817 at a level of $\sim 4\sigma$ below the mean.

At the distance of GW170817, GCs would appear unresolved or marginally resolved in our *HST* imaging depending on the signal-to-noise ratio of the source. To compare the *HST* limit to the luminosities of GCs, we adopt the globular cluster luminosity function (GCLF) derived from prior ACS/F606W imaging. The GCLF is characterized by a Gaussian in magnitude space with a mean and width of $m_{F606W} = 25.45 \pm 0.69$ mag (Lee et al. 2018). Using $M_{\odot,F606W} = 4.72$ mag (Willmer 2018), this translates to $\log(L/L_\odot) = 4.92 \pm 0.27$. Adopting a mass-to-light ratio of $\approx 2\, M_\odot/L_\odot$ (Strader et al. 2009; Baumgardt 2017) the globular cluster mass function (GCMF) can be approximated as a Gaussian with a mean and width of $\log(M/M_\odot) = 5.22 \pm 0.27$. We note that we do not carry out an independent GCLF determination based on our imaging as this would yield incremental returns compared to Lee et al. (2018), due to the difficulty in confirming the GC nature of sources well below the GCLF peak.

With our deep *HST* observation at ≈ 584 days, we place a constraint of $M_{F606W} \gtrsim -4.8$ mag, or $L \lesssim 6.7 \times 10^3\, L_\odot$, on any underlying cluster. It is instructive to compare this limit to the GCMF as generally the rate of in-cluster interactions, and thus mergers, increases with cluster mass (Pooley et al. 2003). A comparison to the GCMF of NGC 4993 places a limit of $M_{GC} \lesssim 1.3 \times 10^4\, M_\odot$, $\approx 4\sigma$ below the mean; only $\approx 0.004\%$ of the total mass in GCs in NGC 4993 is below this limit (Figure 6). This limit is also constraining enough to rule out $\approx 70\%$ of the mass function of young massive clusters, corroborating the lack of any young stellar populations in the galaxy (Portegies Zwart et al. 2010; Blanchard et al. 2017; Levan et al. 2017).

To place this limit in the context of previous limits from cosmological short GRBs, we search for the deepest available optical limits on persistent sources from low-redshift ($z \lesssim 0.3$) events obtained from previous optical imaging. We find that the most constraining limit is from GRB 050709 at $z = 0.161$

(Fox et al. 2005), which corresponds to $M \lesssim 4.5 \times 10^6\, M_\odot$, $\approx 5\sigma$ above the GCMF mean for NGC 4993[21] (Figure 6). Thus, while short GRBs remain too distant to offer a firm conclusion on progenitor formation channels from direct imaging, the deep observations presented here place a direct and strong constraint on an in situ GC origin for a binary neutron star merger. While previous limits have been placed on an existing GC using more shallow, pre-explosion imaging (Blanchard et al. 2017; Levan et al. 2017; Pan et al. 2017) as well as indirect inference from the fading behavior of the afterglow (Lamb et al. 2019a), our analysis provides the deepest existing limit based on direct imaging of the event location.

Finally, we explore the possibility that the progenitor system of GW170817 was formed in a GC and ejected before merger (e.g., Bae et al. 2014; Andrews & Mandel 2019), using the median-subtracted 2019 March observation to identify nearby potential GCs. Using aperture photometry, we identify six sources with $\gtrsim 3\sigma$ significance within a projected distance of $\lesssim 400$ pc ($\lesssim 2''.1$). One of the sources clearly has an extended PSF (previously identified as a GC candidate in Pan et al. 2017) and is most likely a background galaxy, while the five remaining sources are too faint to constrain their PSFs. If they are in fact GCs, their inferred masses are $\approx (1-4) \times 10^4\, M_\odot$ and contain at most $\approx 0.5\%$ of the GC mass of NGC 4993, making it unlikely for the progenitor to have formed there. In general, the progenitor system would have to travel at a minimum of the escape velocity of the GC, a few tens of km s^{-1} for typical GC masses and sizes, and for a potentially long and uncertain merger timescale. Coupled with the old stellar population of the host galaxy, ≈ 11 Gyr (Blanchard et al. 2017), it would thus be extremely challenging to correlate GW170817 with its parent GC.

Looking forward, *HST* imaging to similarly deep limits of future well-localized gravitational-wave events will provide meaningful limits on an in situ GC origin to 200 Mpc (assuming that the GCMF across galaxies is fairly constant; cf. Strader et al. 2006). Specifically, *HST* observations to ≈ 28.5 mag for events at $\lesssim 100$ Mpc ($\lesssim 200$ Mpc) will be sensitive to $\gtrsim 95\%$ ($\gtrsim 30\%$) of the GCMF (Figure 6).

5. Conclusions and Future Outlook

We present the first observation following GW170817 in which an optical source is not detected to deep limits, allowing us to determine the complete F606W light curve of its optical afterglow from ≈ 110 to 584 days. The afterglow evolution is fully consistent with the optical emission emanating from a relativistic structured jet at an observer angle of $\approx 30°$, as indicated by radio and X-ray observations. This study highlights the importance of template observations in determining accurate light curves, especially for the late and faintest stages of evolution. This is especially important for local events detected by gravitational-wave facilities that are embedded in their host galaxies, for which galactic low surface brightness features are more prominent and cannot be easily modeled.

We also compare GW170817 to on-axis cosmological short GRBs. Extrapolating the optical post-peak temporal evolution of GW170817 to the luminosities of short GRBs, the predicted jet break times for short GRBs are consistent with their

---

[21] We note that for the less-massive star-forming host galaxy of GRB 050709, the peak of its GCMF is expected to be similar, while the width may be narrower (e.g., Brodie & Strader 2006). In this case, the limit would correspond to $\gtrsim 5\sigma$ when compared to the GCMF of its host galaxy.

observed breaks. Thus, we find that the two populations can be easily connected if their explosion properties (e.g., energetics, circummerger densities, and jet opening angles) are similar, and that the factor that primarily dictates their different evolution is the observer angle. Continued studies of short GRBs to $\gtrsim 5$ days, as well as similarly in-depth studies of local binary neutron star mergers, will continue to shed light on any intrinsic differences in these populations.

We provide a deep and direct constraint on the presence of an underlying GC to $M \lesssim 1.3 \times 10^4 M_\odot$, providing direct evidence that GW170817 did not form and merge in a cluster in situ at the 4σ level. However, we cannot place meaningful constraints on the possibility that the progenitor system was dynamically formed and ejected from its parent cluster. Future simulations that calculate accurate rates of such systems taking into account the full cluster evolution, coupled with further observational constraints on mergers at $\lesssim 200$ Mpc, will help to elucidate this formation channel.

Finally, we remark that *HST* had a singular role in the optical afterglow of the relatively nearby GW170817. As gravitational-wave facilities increase in sensitivity, most binary neutron star mergers will be detected farther away. If the optical luminosity of the GW170817 afterglow is representative, the advent of extremely large telescopes and future space-based initiatives, such as the *James Webb Space Telescope* will play an incredibly important role in the detection and characterization of off-axis afterglows from binary neutron star (and neutron star–black hole) mergers.

ORCID iDs

W. Fong ⓘ https://orcid.org/0000-0002-7374-935X
P. K. Blanchard ⓘ https://orcid.org/0000-0003-0526-2248
K. D. Alexander ⓘ https://orcid.org/0000-0002-8297-2473
J. Strader ⓘ https://orcid.org/0000-0002-1468-9668
R. Margutti ⓘ https://orcid.org/0000-0003-4768-7586
V. A. Villar ⓘ https://orcid.org/0000-0002-5814-4061
Y. Wu ⓘ https://orcid.org/0000-0002-5347-9225
C. S. Ye ⓘ https://orcid.org/0000-0001-9582-881X
E. Berger ⓘ https://orcid.org/0000-0002-9392-9681
P. S. Cowperthwaite ⓘ https://orcid.org/0000-0002-2478-6939
T. Eftekhari ⓘ https://orcid.org/0000-0003-0307-9984
C. Guidorzi ⓘ https://orcid.org/0000-0001-6869-0835
T. Laskar ⓘ https://orcid.org/0000-0003-1792-2338
A. Macfadyen ⓘ https://orcid.org/0000-0002-0106-9013
B. D. Metzger ⓘ https://orcid.org/0000-0002-4670-7509
M. Nicholl ⓘ https://orcid.org/0000-0002-2555-3192
K. Paterson ⓘ https://orcid.org/0000-0001-8340-3486
G. Terreran ⓘ https://orcid.org/0000-0003-0794-5982
D. J. Sand ⓘ https://orcid.org/0000-0003-4102-380X
P. K. G. Williams ⓘ https://orcid.org/0000-0003-3734-3587
X. Xie ⓘ https://orcid.org/0000-0001-8470-2779
J. Zrake ⓘ https://orcid.org/0000-0002-1895-6516

References

Abbott, B. P., Abbott, R., Abbott, T. D., et al. 2017a, PhRvL, 119, 161101
Abbott, B. P., Abbott, R., Abbott, T. D., et al. 2017b, ApJL, 848, L12
Abbott, B. P., Abbott, R., Abbott, T. D., et al. 2017c, ApJL, 850, L40
Alexander, K. D., Margutti, R., Blanchard, P. K., et al. 2018, ApJL, 863, L18
Anderson, S. B., Gorham, P. W., Kulkarni, S. R., Prince, T. A., & Wolszczan, A. 1990, Natur, 346, 42
Andreoni, I., Ackley, K., Cooke, J.., et al. 2017, PASA, 34, e069
Andrews, J. J., & Mandel, I. 2019, ApJL, 880, L8
Arcavi, I., Hosseinzadeh, G., Howell, A. D., et al. 2017, Natur, 551, 64
Bae, Y.-B., Kim, C., & Lee, H. M. 2014, MNRAS, 440, 2714
Baumgardt, H. 2017, MNRAS, 464, 2174
Becker, A. 2015, HOTPANTS: High Order Transform of PSF ANd Template Subtraction, Astrophysics Source Code Library, ascl:1504.004
Bennett, C. L., Larson, D., Weiland, J. L., & Hinshaw, G. 2014, ApJ, 794, 135
Berger, E. 2014, ARA&A, 52, 43
Bertin, E., & Arnouts, S. 1996, A&AS, 117, 393
Blanchard, P. K., Berger, E., Fong, W., et al. 2017, ApJL, 848, L22
Bohlin, R. C. 2016, AJ, 152, 60
Brodie, J. P., & Strader, J. 2006, ARA&A, 44, 193
Burrows, D. N., Grupe, D., Capalbi, M., et al. 2006, ApJ, 653, 468
Cantiello, M., Jensen, J. B., Blakeslee, J. P., et al. 2018, ApJL, 854, L31
Chambers, K. C., Magnier, E. A., Metcalfe, N., et al. 2016, arXiv:1612.05560
Chornock, R., Berger, E., Kasen, D., et al. 2017, ApJL, 848, L19
Coulter, D. A., Foley, R. J., Kilpatrick, C. D., et al. 2017, Sci, 358, 1556
Cowperthwaite, P. S., Berger, E., Villar, V. A., et al. 2017, ApJL, 848, L17
D'Avanzo, P., Campana, S., Salafia, O. S., et al. 2018, A&A, 613, L1

Deustua, S. E., & Mack, J. 2017, Comparing the ACS/WFC and WFC3/UVIS Calibration and Photometry, Instrument Science Report WFC3 2018-02, (Baltimore, MD: STScI)

Díaz, M. C., Macri, L. M., Garcia Lambas, D., et al. 2017, ApJL, 848, L29

Dobie, D., Kaplan, D. L., Murphy, T., et al. 2018, ApJL, 858, L15

Drout, M. R., Piro, A. L., Shappee, B. J., et al. 2017, Sci, 358, 1570

Fong, W., Berger, E., Blanchard, P. K., et al. 2017, ApJL, 848, L23

Fong, W., Berger, E., Margutti, R., et al. 2012, ApJ, 756, 189

Fong, W., Berger, E., Margutti, R., & Zauderer, B. A. 2015, ApJ, 815, 102

Fong, W., Berger, E., Metzger, B. D., et al. 2014, ApJ, 780, 118

Fox, D. B., Frail, D. A., Price, P. A., et al. 2005, Natur, 437, 845

Ghirlanda, G., Salafia, O. S., Paragi, Z., et al. 2019, Sci, 363, 968

Gonzaga, S. E., Hack, W., Fruchter, A., & Mack, J. 2012, The DrizzlePac Handbook (Baltimore, MD: STScI)

Granot, J., & Sari, R. 2002, ApJ, 568, 820

Grindlay, J., Portegies Zwart, S., & McMillan, S. 2006, NatPh, 2, 116

Ivanova, N., Heinke, C. O., Rasio, F. A., Belczynski, K., & Fregeau, J. M. 2008, MNRAS, 386, 553

Kasliwal, M. M., Nakar, E., Singer, L. P., et al. 2017, Sci, 358, 1559

Kathirgamaraju, A., Barniol Duran, R., & Giannios, D. 2018, MNRAS, 473, L121

Kathirgamaraju, A., Tchekhovskoy, A., Giannios, D., & Barniol Duran, R. 2019, MNRAS, 484, L98

Lamb, G. P., Lyman, J. D., Levin, A. J., et al. 2019a, ApJL, 870, L15

Lamb, G. P., Tanvir, N. R., Levan, A. J., et al. 2019b, arXiv:1905.02159

Lazzati, D., Perna, R., Morsony, B. J., et al. 2018, PhRvL, 120, 241103

Lee, M. G., Kang, J., & Im, M. 2018, ApJL, 859, L6

Lee, W. H., Ramirez-Ruiz, E., & van de Ven, G. 2010, ApJ, 720, 953

Levan, A. J., Lyman, J. D., Tanvir, N. R., et al. 2017, ApJL, 848, L28

Lin, E.-T., Yu, H.-F., & Kong, A. K. H. 2019, JHEAp, 21, 1

Lipunov, V. M., Gorbovskoy, E., Kornilov, V. G., et al. 2017, ApJL, 850, L1

Lyman, J. D., Lamb, G. P., Levan, A. J., et al. 2018, NatAs, 2, 751

Lyman, J. D., Levan, A. J., Tanvir, N. R., et al. 2017, MNRAS, 467, 1795

Margutti, R., Alexander, K. D., Xie, X., et al. 2018, ApJL, 856, L18

Metzger, B. D., Martínez-Pinedo, G., Darbha, S., et al. 2010, MNRAS, 406, 2650

Mooley, K. P., Deller, A. T., Gottlieb, O., et al. 2018a, Natur, 561, 355

Mooley, K. P., Frail, D. A., Dobie, D., et al. 2018b, ApJL, 868, L11

Mooley, K. P., Nakar, E., Hotokezaka, K., et al. 2018c, Natur, 554, 207

Nicholl, M., Berger, E., Kasen, D., et al. 2017, ApJL, 848, L18

Nynka, M., Ruan, J. J., Haggard, D., & Evans, P. A. 2018, ApJL, 862, L19

Palmese, A., Hartley, W., Tarsitano, F., et al. 2017, ApJL, 849, L34

Pan, Y. C., Kilpatrick, C. D., Simona, J. D., et al. 2017, ApJL, 848, L30

Peng, C. Y., Ho, L. C., Impey, C. D., & Rix, H. W. 2010, AJ, 139, 2097

Pian, E., D'Avanzo, P., Benetti, S., et al. 2017, Natur, 551, 67

Piro, L., Troja, E., Zhang, B., et al. 2019, MNRAS, 483, 1912

Pooley, D., Kumar, P., Wheeler, J. C., & Grossan, B. 2018, ApJL, 859, L23

Pooley, D., Lewin, W. H. G., Anderson, S. F., et al. 2003, ApJL, 591, L131

Portegies Zwart, S. F., McMillan, S. L. W., & Gieles, M. 2010, ARA&A, 48, 431

Pozanenko, A., Volnova, A., Mazaeva, E., et al. 2017, A&AC, 1, 8

Rhoads, J. E. 1999, ApJ, 525, 737

Ruan, J. J., Nynka, M., Haggard, D., Kalogera, V., & Evans, P. 2018, ApJL, 853, L4

Salafia, O. S., Ghirlanda, G., Ascenzi, S., & Ghisellini, G. 2019, A&A, 628, A18

Sari, R., Piran, T., & Halpern, J. P. 1999, ApJL, 519, L17

Sari, R., Piran, T., & Narayan, R. 1998, ApJL, 497, L17

Schlafly, E. F., & Finkbeiner, D. P. 2011, ApJ, 737, 103

Sirianni, M., Jee, M. J., Benítez, N., et al. 2005, PASP, 117, 1049

Smartt, S. J., Chen, T.-W., Jerkstrand, A., et al. 2017, Natur, 551, 75

Soares-Santos, M., Holz, D. E., Annis, J., et al. 2017, ApJL, 848, L16

Soderberg, A. M., Berger, E., Kasliwal, M., et al. 2006, ApJ, 650, 261

Strader, J., Brodie, J. P., Spitler, L., & Beasley, M. A. 2006, AJ, 132, 2333

Strader, J., Smith, G. H., Larsen, S., Brodie, J. P., & Huchra, J. P. 2009, AJ, 138, 547

Tanvir, N. R., Levan, A. J., González-Fernández, C., et al. 2017, ApJL, 848, L27

Tauris, T. M., Kramer, M., Freire, P. C. C., et al. 2017, ApJ, 846, 170

Tody, D. 1986, Proc. SPIE, 627, 733

Tody, D. 1993, in ASP Conf. Ser. 52, Astronomical Data Analysis Software and Systems II, ed. R. J. Hanisch, R. J. V. Brissenden, & J. Barnes (San Francisco, CA: ASP), 173

Troja, E., Castro-Tirado, A. J., Becerra Gonzalez, J., et al. 2019a, arXiv:1905.01290

Troja, E., Piro, L., Ryan, G., et al. 2018a, MNRAS, 478, L18

Troja, E., Piro, L., van Eerten, H., et al. 2017, Natur, 551, 71

Troja, E., Ryan, G., Piro, L., et al. 2018b, NatCo, 9, 4089

Troja, E., Sakamoto, T., Cenko, S. B., et al. 2016, ApJ, 827, 102

Troja, E., van Eerten, H., Ryan, G., et al. 2019b, MNRAS, Advance Access

Utsumi, Y., Tanaka, M., Tominaga, N., et al. 2017, PASJ, 69, 101

Valenti, S., Sand, D. J., Yang, S., et al. 2017, ApJL, 848, L24

van Eerten, H. J., & MacFadyen, A. I. 2012, ApJ, 751, 155

Villar, V. A., Guillochon, J., Berger, E., et al. 2017, ApJL, 851, L21

Willmer, C. N. A. 2018, ApJS, 236, 47

Wong, T.-W., Willems, B., & Kalogera, V. 2010, ApJ, 721, 1689

Wu, Y., & MacFadyen, A. 2018, ApJ, 869, 55

Wu, Y., & MacFadyen, A. 2019, ApJL, 880, L23

Zrake, J., Xie, X., & MacFadyen, A. 2018, ApJL, 865, L2